

Buckling of a linear chain of hard spheres in a harmonic confining potential: Numerical and analytical results for low and high compression

Stefan Hutzler^{1,*}, Adil Mughal,² John Ryan-Purcell¹, Ali Irannezhad¹, and Denis Weaire¹

¹*School of Physics, Trinity College Dublin, Dublin 2, Ireland*

²*Department of Mathematics, Aberystwyth University, Penglais, Aberystwyth, Ceredigion, Wales SY23, United Kingdom*



(Received 25 May 2020; accepted 24 July 2020; published xxxxxxxxx)

We extend a previous analysis of the buckling properties of a linear chain of hard spheres between hard walls under transverse harmonic confinement. Two regimes are distinguished—low compression, for which the entire chain buckles, and higher compression, for which there is localized buckling. With further increase of compression, second-neighbor contacts occur; beyond this compression the structure is no longer planar, and is not treated here. A continuous model is developed which is amenable to analytical solution in the low compression regime for an infinite chain. This is helpful in understanding the scaling properties of both finite and infinite chains.

DOI: 10.1103/PhysRevE.00.002900

I. INTRODUCTION

In this paper we examine an elementary problem: the buckling of a linear chain of hard spheres. The spheres are confined between opposing hard walls while also being confined in the transverse direction by a cylindrically symmetric potential which is zero along an axis perpendicular to the two hard walls. The linear chain is unstable under the slightest compression and forms a range of buckled zigzag structures with increasing compression. Below a critical compression the structure remains planar and it is this regime which we study using simulations and experiments. At higher compressions, more complex three-dimensional structures emerge. A description in terms of disks is natural for the theory, but we will use the term “spheres” throughout, as a reminder of the nature of the relevant experiments.

Our paper bears many similarities to studies of the jamming of disks in a narrow channel [1–3]; an extension to the jamming of disks in a centrifuge, similar to the confining harmonic potential presented in this paper, was carried out in [4]. However, the approach in these studies is usually a statistical one, using methods such as Monte Carlo simulations [5] to find jammed structures. Our method relies on a recursion relation. This has the advantage of being simple and amenable to both numerical and analytical treatment.

Despite its simplicity such a model can stand as a tractable prototype for a more general class of physical systems that include soft particles and/or long-range interactions. We expect this paper to find applications in a range of experiments involving zigzagging linear chains of particles. Examples include cold ions in traps [6–12], dusty plasmas [13], droplets in microfluidic crystals [14], paramagnetic colloidal

particles in an external field [15], and linear chains of magnetic spheres [16,17].

Following up on a preliminary investigation of the initial stage of buckling [18], here we will analyze it more exhaustively and adduce a new *continuous* model for low compression properties of the discrete chain.

We will examine two kinds of bifurcation diagrams that represent the proliferation of alternative equilibria (both stable and unstable) at higher compression. The first of these diagrams deals with relative energy and is an improved version of that previously reported [18]. The second represents the position at which buckling is localized for each of the alternative equilibrium states. If each branch of such a bifurcation diagram is pursued to higher compressions it terminates, in the sense that second-nearest neighbors come into contact; the structure becomes nonplanar, and the methods used here are inadequate. Anything beyond this is therefore reserved for further studies, as is the exploration of buckling properties of soft spheres and the determination of Peierls-Nabarro potentials.

Figure 1 shows an illustrative example from an elementary experiment, described in detail in Sec. VIII.

In the following we begin by describing the model and the numerical scheme that we use, after which we present detailed results from simulations for the buckling of a linear chain of $N = 5, 6, 7,$ and 8 hard spheres. In the limit of low compressions we adduce analytical results, based on a continuous approximation, which are compared with simulations. Finally, we present exemplary experiments, which are directly compared with simulations.

II. UNIFORM ZIGZAG

Before giving the details of our methods we describe the closely related case of the *uniform zigzag* arrangement of hard spheres, which is the equilibrium arrangement if periodic boundary conditions are applied to a finite chain (with an even number of spheres), as shown in Fig. 2. The analysis of

*Present address: stefan.hutzler@tcd.ie; School of Physics, Trinity College Dublin, Dublin 2, Ireland.

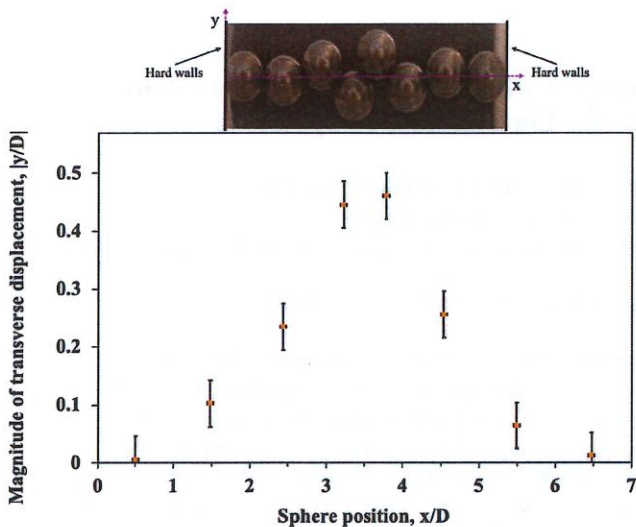


FIG. 1. Photograph of an elementary experiment (described in Sec. VIII) showing a chain of $N = 8$ hard spheres under compression. Also shown are the magnitudes of the transverse displacements of the sphere centers. Both the values for position and displacement relative to the center are normalized by the sphere diameter. (The presence of oil in the plastic cylinder, included to reduce friction, leads to an optical distortion in the photograph; the measured ratio of sphere extension to sphere diameter ($D = 6.33$ mm) in x and y directions is about 0.98 and 1.11, respectively). The error bars in this figure represent the uncertainty in the measurement of the sphere centers using IMAGEJ [23]. The error is ± 0.04 of a sphere diameter in both the x and y directions.

III. MODEL AND METHOD

We are concerned with a system of N hard spheres of unit diameter, confined between hard walls. The confining force at the walls (an important quantity in all later calculations) is G_0 . In contact but uncompressed, the chain is of length $L = N$. For $G_0 > 0$ the compression will be represented by the parameter

$$\Delta = N - L. \tag{1}$$

The total energy is given by

$$E = \frac{1}{2} \sum_{n=1}^N y_n^2, \tag{2}$$

where y_n is the transverse displacement of the n th sphere from the central axis (for details of how the nondimensional quantities are derived see [18]). Note that the model is confined to be planar because only planar structures are found in the regime that we explore, as may be confirmed by energy minimization calculations not confined to two dimensions [19].

We search for equilibrium structures (stable or unstable): each sphere is in equilibrium under the action of contact forces and the confining force associated with the potential energy, given in Eq. (2). We do so by the same shooting method adopted in [18]. This uses the following recursion relations to proceed from one wall to the other and searches for solutions consistent with both hard wall boundary conditions. The relations are

$$\theta_{n+1} = \arctan \left(\frac{F_n}{G_0} - \tan \theta_n \right), \tag{3}$$

$$F_{n+1} = \sin \left[\arctan \left(\frac{F_n}{G_0} - \tan \theta_n \right) \right] - F_n. \tag{4}$$

Figure 3 illustrates the significance of the parameters in Eqs. (3) and (4): F_n is the force due to the harmonic potential on the n th sphere, and θ_n is the tilt angle (i.e., the angle between the line connecting the centers of spheres $n - 1$ and n and the central axis). Note that both F_n and θ_n are defined in such a way as to always be positive. The direction in which they are measured alternates from one sphere to the next. All structures that are found are of a “zigzag” character, that is, with alternating signs of displacement and angle (for a photograph of an example see Fig. 1), but not uniform. G_0 is also positive and is the force exerted on each of the hard walls, normal to the wall.

The hard wall boundary condition for sphere $n = 1$ requires the first tilt angle θ_1 to be zero. For a chosen value of G_0 , we proceed iteratively from an initial choice of F_1 to (F_{N+1}, θ_{N+1}) . The angle θ_{N+1} corresponds to the contact of the N th sphere with the wall, as illustrated in Fig. 3. We search for values of F_1 (in general more than one) such that the angle θ_{N+1} is zero, satisfying the second hard wall boundary condition. Note that the resulting solution is for given G_0 , fixed during the iteration; compression Δ is not preset, but rather given as an output.

This search is performed by coarse graining the initial force F_1 over a range of $0 < F_1 \leq 0.5$ in steps of 10^{-4} . These values are then used as brackets in a bisection method. An exception to this is required when searching for a solution close to the termination points (marking contact formation between

the uniform zigzag is very elementary. All of the structures discussed below are modulated versions of it, conforming to hard wall boundary conditions at the two ends of the chain. For any given axial compression the uniform zigzag structure can be characterized by a lateral displacement y which is the same for each sphere, and an angle θ . Between contacting spheres there is a compressive force G (with no friction)—its horizontal component is $G_0 = G \cos \theta = \frac{1}{4}$ (in nondimensional units; see [18]).

The uniform zigzag is an equilibrium solution for any compatible boundary conditions but it is always unstable, except for very small N . If released from the condition of uniformity, it will undergo the localization that is the subject of this paper, in order to reach a stable state. See the Appendix.

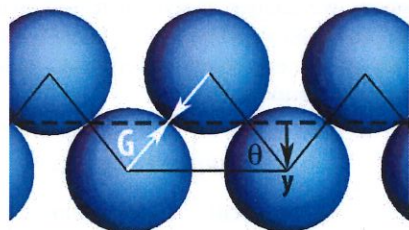


FIG. 2. The uniform zigzag structure is characterized by the same transverse displacement y and tilt angle θ for each sphere. There exists a compressive force G between all contacting spheres.

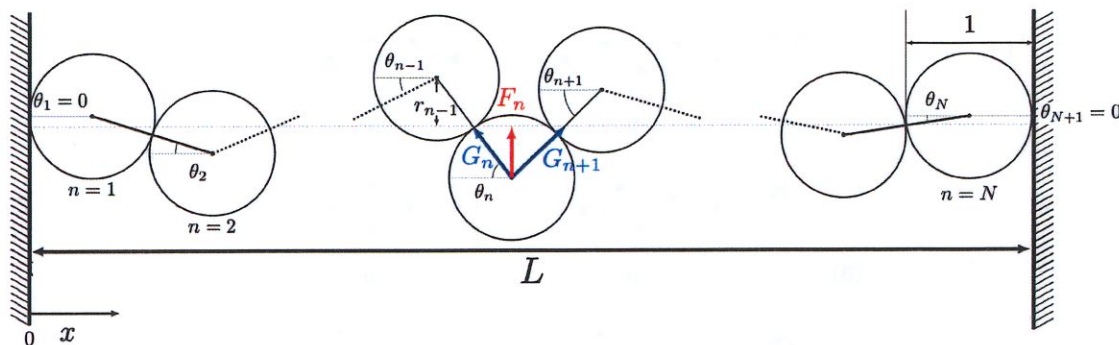


FIG. 3. Schematic for the analysis of a chain of hard spheres under compression, showing the role of the contact forces G_n , restoring forces F_n (equal to the transverse displacements y_n in the units used here), and contact angle θ_n . The horizontal coordinate of the center of each sphere x_n relates to the middle.

next-nearest-neighbor spheres) for a given structure (as described in Sec. IV). This regime was found to require smaller steps and enhanced accuracy.

Given any equilibrium structure determined in this way, we may compute the compression Δ , as

$$\Delta = N - \sum_{n=1}^N \cos \theta_n, \quad (5)$$

together with other quantities of interest. Some of these quantities are as follows.

The total energy E , Eq. (2), is an obvious choice. When we compare different buckled structures for the same compression, the difference of their energies will be relatively small. Accordingly we will adopt a definition of *relative energy*, given in Sec. IV.

Another useful output quantity is the value of the maximum displacement, here equal to F_{\max} . We shall mainly use the tilt angle θ_n as a measure of local buckling.

The position of the peak (maximum transverse displacement) of a buckled chain is defined by the following weighted average of squared displacements:

$$x_p = \frac{\sum_n F_n^2 (x_n - L/2)}{\sum_n F_n^2}, \quad (6)$$

where N is the number of spheres, x_n and y_n (in the nondimensional units used here, $y_n = F_n$) give the position of the n th sphere, and L is the chain length.

The width w of the peak is then defined as

$$w = 2 \sqrt{\frac{\sum_n F_n^2 (x_n - x_p)^2}{\sum_n F_n^2}}. \quad (7)$$

The shooting method described above is so efficient that very large amounts of data are easily generated in order to compile, for example, the comprehensive bifurcation diagrams presented below.

IV. EXAMPLES OF EQUILIBRIUM STRUCTURES AND BIFURCATION DIAGRAMS

At very low compression, equilibrium structures are *symmetric* about the midpoint between the two walls. The basic symmetry of the system requires that either this is the case or

the structures occur as equivalent pairs, related by reflection about the center of the system. Figure 1 was an example of this. At higher compressions, asymmetric structures arise in pairs with positions $x_p = \pm x$.

In this section examples of equilibrium structures are shown and located on the relevant bifurcation diagrams.

There is no difficulty in applying the method to large values of N , of the order of 10^2 or more, but for present purposes of building up a clear picture of localization properties it is preferable to use small values. We have chosen $N = 5, 6, 7$, and 8 as illustrations, in each case computing bifurcation diagrams and showing representative examples of equilibrium structures.

As already noted in [18], there is a distinct difference between systems of *odd* or *even* N as regards the stability or instability of the symmetric states. We shall discuss this for the examples that follow.

A. The case $N = 5$

A representative sample of equilibrium structures for a system with $N = 5$ is shown in Fig. 4(a). Unstable structures are marked with an asterisk.

The bifurcation diagram Fig. 4(b) shows the position of the buckling peak [as found by using Eq. (6)] against the compression Δ . Note that this is only half of the complete diagram, the other half being obtained by reflection in the horizontal axis. (See the above remark concerning symmetry.)

With the exception of the symmetric structure S (see below) the solutions found by the shooting method are labeled alphabetically in ascending order as indicated in Fig. 4(b).

For low values of compression Δ the only solution is S , the symmetric structure, with buckling located at the midpoint of the chain. This solution is shown by the red line along the horizontal axis in Fig. 4(b). An example of such a solution is shown in Fig. 4(a) and is labeled S_1 , corresponding to point indicated in Fig. 4(b).

With increasing compression the structure B emerges by a pitchfork bifurcation from the symmetric structure S . The buckling of the structure B is asymmetric, as shown by the image labeled B_1 in Fig. 4(a).

At the onset of the pitchfork bifurcation, the symmetric arrangements becomes unstable and we label it S^* to indicate this. Continuing to compress the unstable symmetric structure

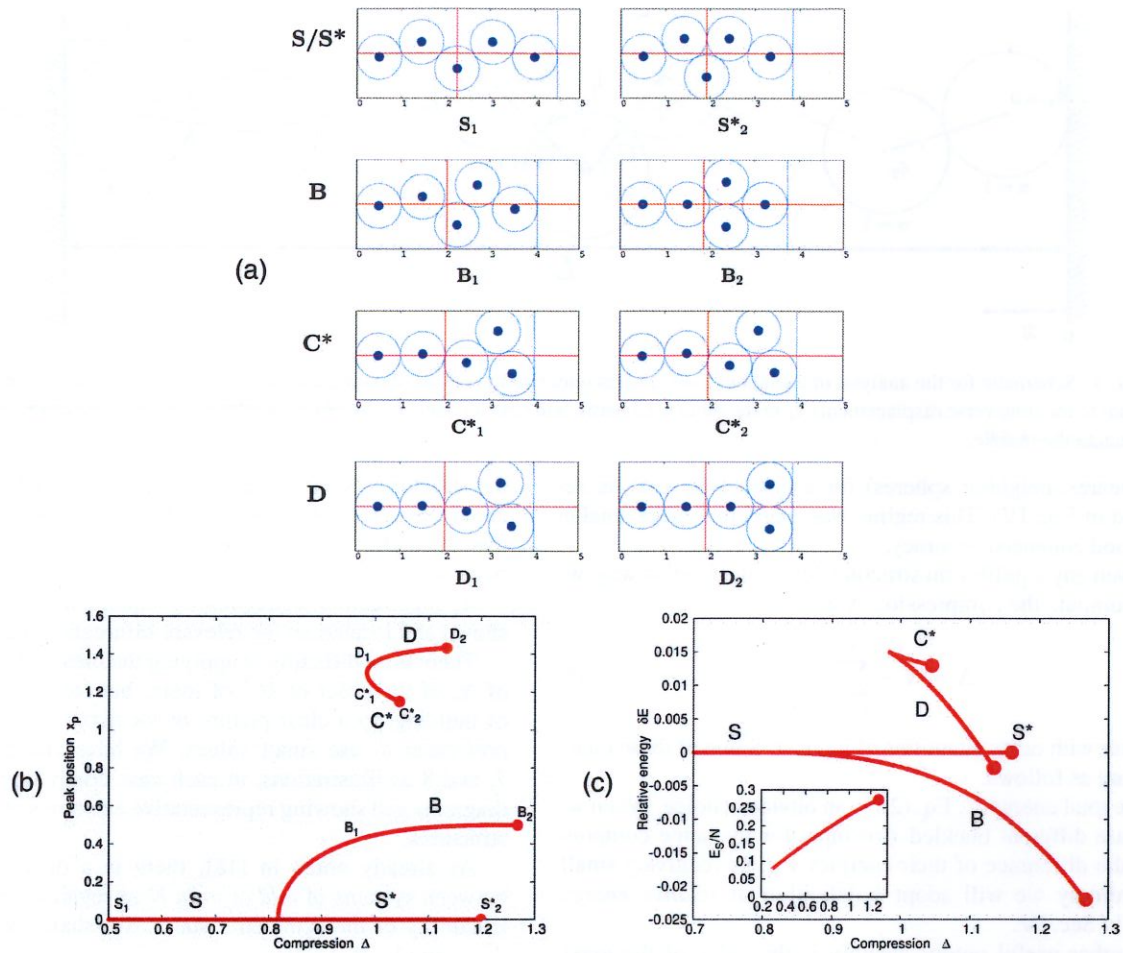


FIG. 4. Results for a chain of $N = 5$ spheres. (a) The linear chain is bounded by two opposing hard walls, at $x = 0$ and L (the second wall is indicated by a vertical dashed blue line). Blue dots indicate sphere centers. The horizontal red line marks $y = 0$ while the vertical red line shows the midpoint of the linear chain (i.e., $x = L/2$). The labels below each structure correspond to the location in the bifurcation diagrams at which that solution is to be found. (b) Bifurcation diagram for peak position and (c) that for energy, relative to that of the symmetric structure. Unstable solutions are marked with an asterisk. The termination point of each branch is shown by a red dot. The inset in (c) shows the energy per sphere of the symmetric structure.

218 further brings the two spheres adjacent to the central sphere
 219 ever closer until they eventually come into contact [S_2^* in
 220 Fig. 4(a)]. At this point we terminate the solution.

221 We indicate all termination points by a red dot, as in
 222 Fig. 4(b). While the present model can be used to follow the
 223 solution beyond such termination points (leading to overlap
 224 between next-nearest-neighbor spheres), we do not show that
 225 unphysical result here.

226 With increasing compression a second pair of solutions
 227 emerges from an “out-of-the-blue” bifurcation, without any
 228 preceding structure. These are labeled C^* and D ; they have
 229 their buckling peaks shifted even further towards the bounding
 230 walls. In the case of D , with increasing compression the
 231 structure eventually tends towards an arrangement with a pair
 232 of spheres against the bounding wall [labeled D_2 , see
 233 Fig. 4(a)].

234 Note that the structures as labeled in Fig. 4(b) alternate in
 235 stability. That is, if the symmetric structure is unstable then
 236 the next structure will be stable, and so on. In our preliminary
 237 work (see [18]) the identification of stable or unstable

238 structures was supported by energy minimization calculations 238
 239 (which gave the stable modes). At this stage such confirmation 239
 240 is not necessary, as the alternating pattern of stable or unstable 240
 241 structures has been established. 241

242 Another quantity of interest is the relative energy of the 242
 243 structures. This we will define as the energy of a solution 243
 244 relative to that of the symmetric structure for the same value 244
 245 of compression Δ : 245

$$\delta E(\Delta) = E(\Delta) - E_{S^*}(\Delta), \quad (8)$$

246 where $E(\Delta)$ is the energy of the structure at a compression 246
 247 Δ and $E_{S^*}(\Delta)$ is the energy of the symmetric structure at 247
 248 the same compression. This is convenient, since the energy 248
 249 difference between all of these structures is very small. The 249
 250 total energy of the symmetric structure is indicated in an inset. 250

251 All of the qualitative features of these results apply to 251
 252 any case of *odd* N , except that the number of asymmetric 252
 253 structures increases with N . 253

254 Note that the bifurcation diagrams presented in [18] used 254
 255 a different (and more convenient) definition. This was the 255

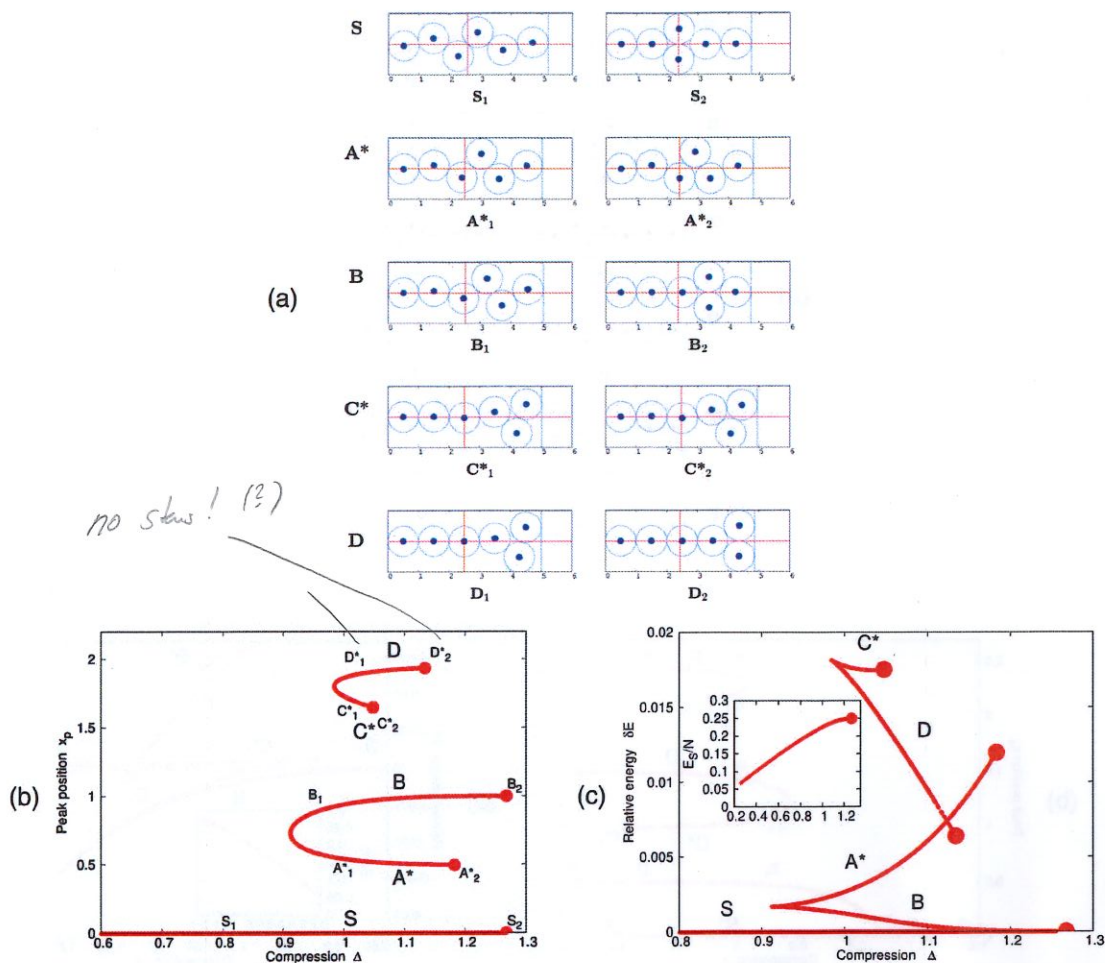


FIG. 5. Results for $N = 6$ spheres. (a) Structures found using the shooting method. (b, c) bifurcation diagrams for peak position and energy, respectively. Again, unstable solutions are indicated with an asterisk. The notation is the same as for Fig. 4.

energy relative to that of the symmetric structure for the same compressive force G_0 .

B. The case $N = 6$

A representative sample of the equilibrium structures for $N = 6$ is shown in Fig. 5(a), together with the accompanying bifurcation diagrams in Figs. 5(b) and 5(c).

In the case of $N = 6$ (or any even N) the symmetric structure S is *always* a stable solution (as it is for all cases where N is even).

We again find that at low compressions the only equilibrium structure is the symmetric one. With increasing compression two new solutions appear from an out-of-the-blue bifurcation as a stable and unstable pair; we label these states A^* and B , that is, in order of the buckling peak position, as shown in Fig. 5(a).

Finally, for larger values of compression a second out-of-the-blue bifurcation yields another stable and unstable pair, which we label C^* and D .

C. The case $N = 7$

A representative sample of the equilibrium structures for $N = 7$ is shown in Fig. 6, with the accompanying bifurcation

diagrams in Figs. 6(b) and 6(c). Since this is a case with an odd value of N the symmetric structure (S) is initially stable and then becomes unstable (S^*) at the pitchfork bifurcation.

D. The case $N = 8$

A representative sample of the equilibrium structures for $N = 8$ is shown in Fig. 7 with the accompanying bifurcation diagrams in Figs. 7(b) and 7(c). Since the value of N is even, the symmetric structure S is always stable.

E. Alternative structures

These bifurcation diagrams are rich in detail, yet they are not to be taken to be complete. As has been noted by others [9–12], there are in principle further structures at higher energies. At the present stage these seem unlikely to have much significance for real physical systems. One may take *multiple* peaks as an example. For large enough Δ they are just simple combinations of single peaks, with some interaction between them. An example of such a structure (generated using the shooting method) with multiple peaks for $N = 10$ is shown in Fig. 8.

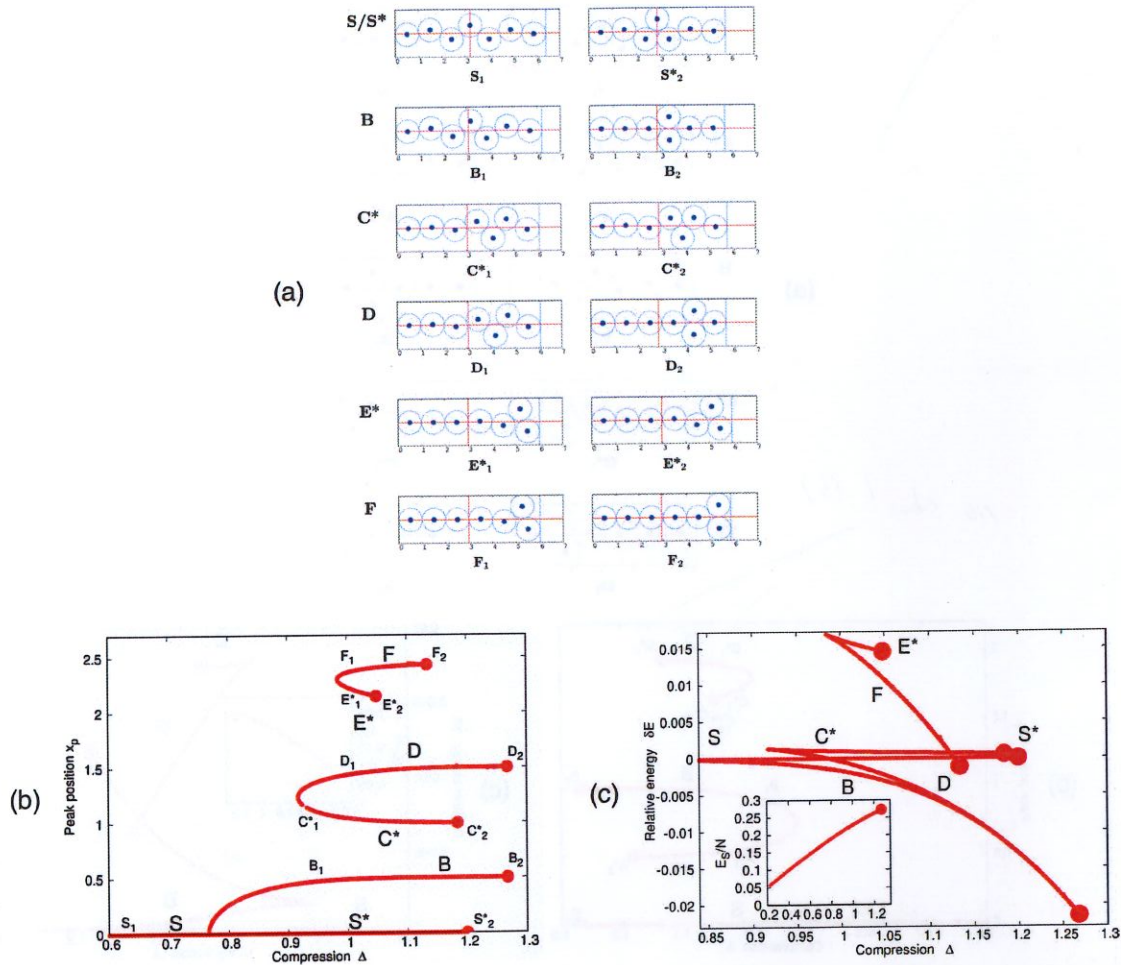


FIG. 6. Results for $N = 7$ spheres. (a) Structures found using the shooting method. (b, c) Bifurcation diagrams. Notation details are the same as for Fig. 4. The disconnected regions apparent in the diagrams for C_1^* and for (b) and the branch of E^* are an artifact of the simulation and in principle can be removed by using a smaller step size.

V. TERMINATION POINTS

296

At each termination point the equilibrium structure acquires at least one new contact. Illustrative examples were already included in Figs. 4–7.

297

298

299

For the symmetric structure, a chain with an even number of spheres takes the terminal form shown in Figs. 5 and 7, while in the case of a chain with an odd number of spheres it takes the form shown in Figs. 4 and 6.

300

301

302

303

We may refer to that of Fig. 5 (or Fig. 7), i.e., the arrangement labeled S_2 , as a *doublet*. This simple equilibrium configuration can clearly be constructed anywhere in the chain, with the same compression $\Delta_{\text{doublet}} = 3 - \sqrt{3} \approx 1.2679$ and energy $E_{\text{doublet}} = 1/4$. The energy variation with Δ as this is approached is found to be quadratic close to the termination point:

304

305

306

307

308

309

310

$$E - E_{\text{doublet}} \sim (\Delta - \Delta_{\text{doublet}})^2. \quad (9)$$

Note also that for hard spheres the compression force G_0 is zero in the case of the doublet, so G_0 increases from 1/4

311

312

(the same value as for the uniform zigzag) to a maximum and declines to zero, as compression Δ is increased from zero.

313

314

In general, asymmetric states appear to tend towards the doublet configuration, but they develop a single additional contact just before it is formed, and at this point we must stop, in the present paper. In a real system a small further compression will bring the second extra contact into play and the perfect doublet structure will be found.

315

316

317

318

319

320

Asymmetric structures with a localized peak next to the wall may tend towards what we call a half doublet (e.g., structure F_2 in Fig. 7).

321

322

323

Once additional contacts have been formed, we enter a new regime, beyond the range of the present paper. With further compression the doublet becomes the nucleus for the development of a new type of structure, which grows in extent until it takes over the whole chain. In reality it is unstable with respect to a *twist*, so the structure becomes three-dimensional, if allowed to do so.

324

325

326

327

328

329

330

It should not be beyond the scope of the recursive method (suitably adapted) to pursue these higher structures, which require a different experimental technique from that shown

331

332

333

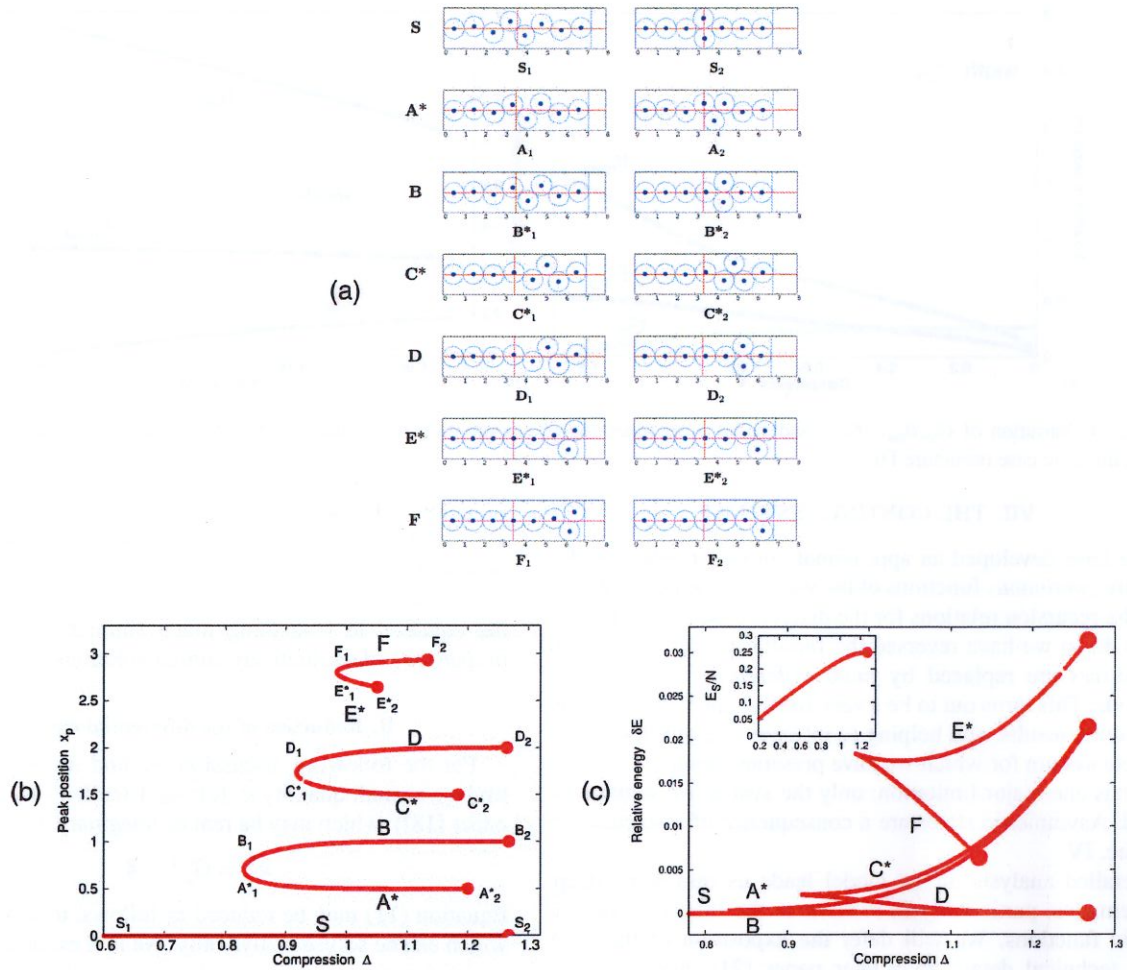


FIG. 7. Results for $N = 8$ spheres. (a) Structures found using the shooting method. (b, c) Bifurcation diagrams. Details of the notation are the same as for Fig. 4.

334 here [18,20]. We intend to undertake this continuation in the
 335 future. It should complement previous investigations [19])
 336 on the full range of three-dimensional structures, which was
 337 based on energy minimization.

338 **VI. DEPENDENCE OF EQUILIBRIUM PROPERTIES ON**
 339 **COMPRESSION FOR A DISCRETE CHAIN**

340 The localized buckling that is observed may be conve-
 341 niently characterized by θ_{\max} , the maximum value of θ . Its
 342 dependence on compression Δ is shown in Fig. 9, for the

343 case of $N = 8$. An initial increase of θ_{\max} that is apparently of
 344 square-root form is followed by a broad linear regime, roughly
 345 speaking, before the terminal regime develops. Also shown
 346 are the variation of G_0 and F_{\max} and the width w , defined in
 347 Sec. III.

348 While it is possible to discuss these variations within the
 349 discrete model, we have found it illuminating to develop a
 350 continuous description which provides relevant analytical re-
 351 sults and approximations, particularly for small compression.
 352 In Sec. VIII we also show experimental results of the variation
 353 of θ_{\max} and width with compression.

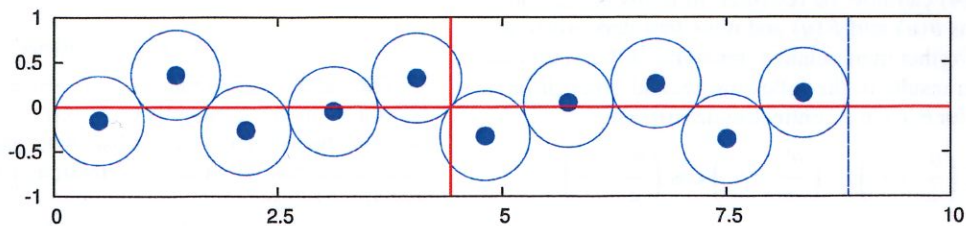


FIG. 8. A linear chain for $N = 10$ displaying multiple peaks of transverse displacement.

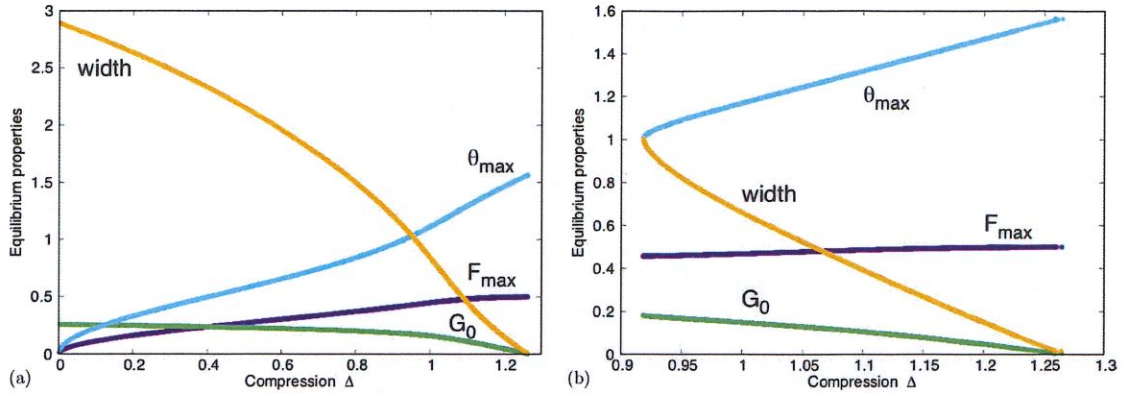


FIG. 9. Variation of G_0 , θ_{\max} , F_{\max} , and width w as functions of compression for a chain of $N = 8$ spheres for the (a) symmetric and (b) asymmetric case (structure D).

VII. THE CONTINUOUS LIMIT

We have developed an approximate model in which θ , F , etc., are *continuous* functions of the variable u , which replaces n in the recursion relations for the discrete case (Sec. III).

To do so we have reversed the familiar process by which *derivatives* are replaced by *finite differences* in numerical methods. This turns out to be a very fruitful approach, leading to analytic results, and helping to interpret the profiles of the discrete system for which we have presented results.

It has one major limitation: only the *symmetric* solution is found. Asymmetric states are a consequence of discreteness: see Sec. IV.

Detailed analysis of the model leads us into some deep mathematics, particularly in relation to the theory of Jacobi elliptic functions. We will defer the exposition of this and other technical details to a later paper [21]: here we will concentrate on its results and their implications.

We shall investigate the continuous formulation for both finite and infinite systems.

A. Transition to the continuous model

The discrete model is described by the difference equations Eqs. (3) and (4). To arrive at a single second-order equation for the angle $\theta(u)$, with $0 \leq u < \infty$ we proceed as follows. We define $\theta(u) = \theta_{n+1} - \theta_n$, corresponding to a finite difference equation for $u = n + 1/2$. Similarly we set $\theta(u) = \frac{1}{2}(\theta_{n+1} + \theta_n)$. Using an equivalent procedure for the introduction of a displacement function $F(u)$ results in

$$F(u) = \frac{1}{2} \sin \left[\theta(u) + \frac{\theta'(u)}{2} \right], \quad (10)$$

where we have made use of Eqs. (3) and (4).

Equation (4) can now be rewritten in terms of the continuous functions $\theta(u)$ and $F(u)$ and their first derivatives with respect to u . Further manipulation, involving differentiation of Eq. (10), then results in the following second-order differential equation for $\theta(u)$ in a continuum description:

$$2 \sin \left(\frac{\theta'}{2} + \theta \right) - \left(\frac{\theta''}{2} + \theta' \right) \cos \left(\frac{\theta'}{2} + \theta \right) - 8G_0 \frac{\sin(2\theta)}{\cos 2\theta + \cos \theta'} = 0. \quad (11)$$

Equation (11) looks unpromising, as it offers little hope of a closed-form solution. Indeed, for present purposes we will present numerical solutions using MATHEMATICA.

In order to make sense of these results it is helpful to reduce the equation to something much simpler, with transparent properties and qualitatively similar solutions.

B. Reduction of the differential equation

For the following discussion we find it convenient to introduce a small quantity κ , $|\kappa|^2 \ll 1$ (called ϵ in our previous paper [18]), which may be real or imaginary, by defining

$$\kappa^2 = G_0^{-1} - 4. \quad (12)$$

Equation (11) may be reduced as follows, to arrive at a form which can be solved analytically. We first expand the sine and cosine functions to second order in θ and θ' . We then evaluate the magnitudes of the various terms involving products of θ , θ' , and θ'' and their powers in terms of the maximum value θ_{\max} (peak) of a solution. The result is the nonlinear differential equation which we refer to as the *first reduced equation*:

$$\theta'' = \kappa^2 \theta - 2\theta^3, \quad \text{for small } \kappa \text{ and } \theta, \quad (13)$$

which has proved to be useful. We will make only limited use of it here, and present a full analysis of its solutions, and further quantitative comparison with those of the full equation, in a further paper. Further reductions yield the *second reduced equation*,

$$\theta'' = \kappa^2 \theta, \quad \text{neglecting the } \theta^3 \text{ term}, \quad (14)$$

and the *first reduced equation* for $\kappa = 0$:

$$\theta'' = -2\theta^3. \quad (15)$$

C. Exact solutions

The value of the reduced (and hence approximate) equations lies in the availability of exact solutions. These will be described in detail in a subsequent paper: they have been used to validate the numerical treatment of the full equation, presented below.

The simplest example is that of the second reduced equation (14), which is linear and has exponential solutions,

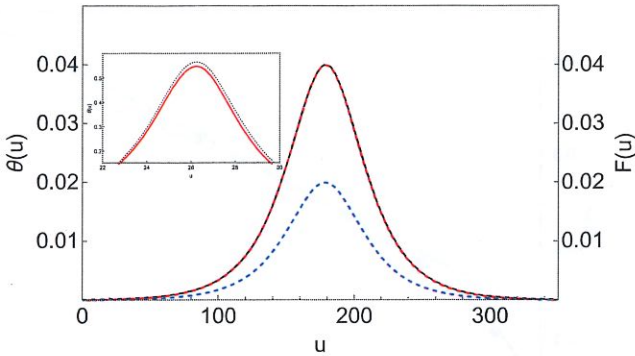


FIG. 10. Profiles of tilt angle $\theta(u)$ (red solid line) and corresponding forces (displacements), $F(u)$ (blue dashed line), as obtained from a numerical solutions of Eq. (11) for an infinite system with $\kappa = 0.04$, resulting in a value for compression $\Delta = 0.0398$. The analytical solution of the first reduced equation, Eq. (17) (dashed black line), provides an excellent approximation for $\theta(u)$. Only for higher values of κ are differences around the peak noticeable, as is seen in the inset for $\kappa = 0.35$, corresponding to compression $\Delta = 0.328$. (Note that the analytical solutions are shifted along the u axis so that their peak positions match those of the numerical solutions.)

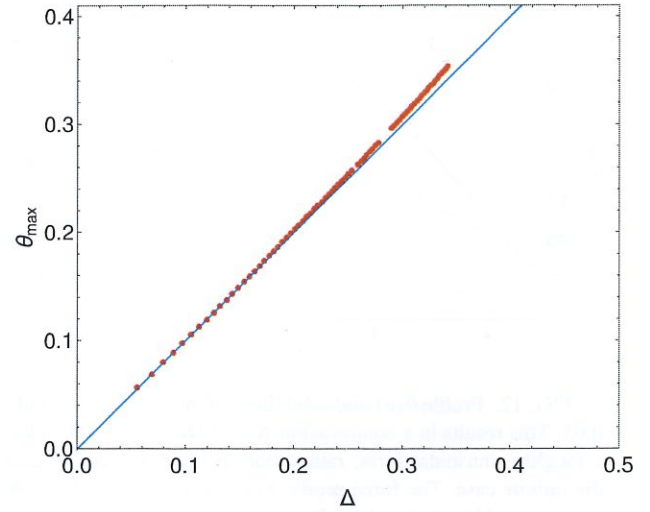


FIG. 11. Variation of θ_{\max} with compression Δ for an infinite system. Data points are from numerical solutions of the full differential equation, Eq. (11). The line of slope unity represents the analytical result obtained for the reduced equation for low compressions, Eq. (19).

419 given by

$$\theta(u) \sim \exp(\pm\kappa u). \quad (16)$$

420 These apply away from the peak, in the tails of the profile for
421 the infinite case, as in Fig. 10.

422 The first reduced equation (13) has much more general
423 applicability, and develops all the features of the solution of
424 the full equation, for low compression. Its exact solution is
425 given by

$$\theta(u) = \kappa \operatorname{sech}(\kappa u). \quad (17)$$

426 The inflection points beyond which the exponential tails de-
427 velop are at $u = (\ln \sqrt{2} \pm 1)/\kappa$.

428 The compression Δ may be evaluated using

$$\Delta = \int_0^\infty [1 - \cos \theta(u)] du. \quad (18)$$

429 Approximating $1 - \cos \theta$ by $\frac{\theta^2}{2}$, we find that

$$\Delta \approx \kappa \approx \theta_{\max} \text{ as } \kappa \rightarrow 0. \quad (19)$$

430 Further exact but less transparent solutions are provided by
431 Jacobi functions which will be fully described in a subsequent
432 publication [21].

433 D. Numerical solutions

434 We have used standard MATHEMATICA routines to compute
435 numerical solutions of the full equation (11) for both infinite
436 and finite systems.

437 1. Infinite system

438 We model the infinite system by defining boundary condi-
439 tions at a position well out in the exponential tail of the
440 solution (here set at $u = 0$). For a given value of κ the
441 conditions then are $\theta(0)/\theta_{\max} = \theta(0)/\kappa \ll 1$, and $\theta'(0) =$
442 $\kappa\theta(0)$, consistent with Eq. (17). From the solution $\theta(u)$ we

443 then obtain the corresponding value for compression Δ by
444 numerically performing the integration of Eq. (18). The force
445 profile is computed from Eq. (10).

446 As an example we show in Fig. 10 tilt angle $\theta(u)$ and
447 force profile $F(u)$ for $\kappa = 0.04$, resulting in a compression
448 $\Delta = 0.03976$. [In this case we found setting $\theta(0) = 10^{-6}\kappa$
449 sufficiently small for independence of the profile from the
450 value of $\theta(0)$.] For this compression the analytic solution of
451 the first reduced equation, Eq. (17), plotted as a dashed black-
452 line, provides an excellent approximation of the numerical
453 solution $\theta(u)$ of the full equation. Deviations of the two
454 solutions become apparent only for larger values of κ , and
455 thus deformation (see the inset in Fig. 10 which was produced
456 for $\kappa = 0.35$, resulting in $\Delta = 0.328$).

457 We have repeated such calculations for a range of values
458 of κ (and thus Δ). Figure 11 shows that in the limit of small
459 compression θ_{\max} varies linearly with Δ , consistent with the
460 analytic result of Eq. (19) deduced from the solution of the
461 first reduced equation, Eq. (17).

462 2. Finite system

463 A finite chain of N spheres confined by hard walls at
464 both end points is represented by $\theta(1) = 0$ and $\theta(N) = 0$.
465 Only the first equation is directly implemented as a boundary
466 condition in our numerical scheme. We have proceeded by
467 setting $\theta'(1) = 2 \arcsin(2F_1)$ [see Eq. (10)] and increasing
468 F_1 in a procedure similar to that used for the discrete case
469 described in Sec. III. We thus search for a value of F_1 so
470 that for a given value of κ the numerical solution of the full
471 equation [Eq. (11)] results in $\theta(N) = 0$.

472 Figure 12 shows an example of the profiles $\theta(u)$ and $F(u)$
473 for $N = 10$ and $\kappa = 0.03$. The corresponding value of com-
474 pression is computed from Eq. (18), resulting in $\Delta = 0.164$.

475 Unlike in the infinite case [Eq. (19)], for finite systems
476 the value of $\kappa = 0$, i.e., $G_0 = 1/4$ [see Eq. (12)], results in a
477

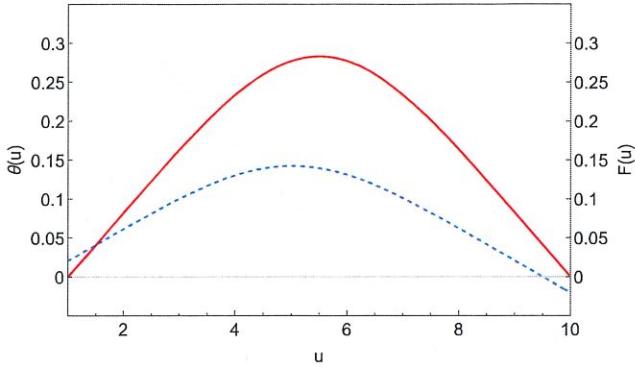


FIG. 12. Profile $\theta(u)$ (red solid line) for the case $N = 10$ and $\kappa = 0.03$. This results in a compression $\Delta = 0.164$. The profile takes on a roughly sinusoidal form, rather than the form of $\text{sech}(u)$ seen in the infinite case. The force profile $F(u)$, obtained from Eq. (10), is shown as a blue dashed line. Its maximum is shifted relative to the maximum of θ , as $\theta'(u)$ is no longer small throughout the solution, as per Eq. (10).

477 nonzero compression Δ . To study the limit $\Delta \rightarrow 0$ we require
 478 values of $G_0 > 1/4$, i.e., $\kappa^2 < 0$, corresponding to imaginary
 479 values of κ (i.e., $\kappa = i\mu$). Solutions at such low compression
 480 have a different qualitative form. Whereas the finite tails
 481 may be approximated by sinh functions at the boundaries for
 482 positive κ (instead of exponentials that we noted in the infinite
 483 case), imaginary κ implies a profile proportional to $\cos(\mu u)$
 484 as $\Delta \rightarrow 0$ [see the second reduced equation, Eq. (14)]. In that
 485 limit we obtain $\frac{\pi}{\mu} = N$, to fit both boundary conditions.

486 Figure 13 shows the variation of κ^2 with Δ , again for the
 487 case $N = 10$, consistent with the above description. While for
 488 the infinite system κ^2 remains positive for all values of Δ ,
 489 there is a crossover to negative values in the case of finite N .

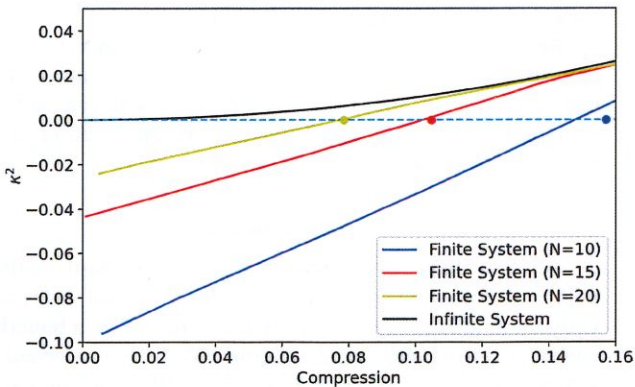


FIG. 13. The variation of κ^2 as a function of compression shows a qualitative difference for the cases of finite or infinite chain. Finite systems [here represented by numerical solutions of the full differential equation, Eq. (11), for $N = 10, 15$, and 20] show a change in the sign of κ^2 . This is accompanied by a change of the functional form of the profiles for $\theta(u)$ and $F(u)$. For the infinite system (Sec. VII D 1) κ remains positive for all values of compression. The points marked on the $\kappa^2 = 0$ line represent predictions from analytic results of the reduced equation (for details see [21]).

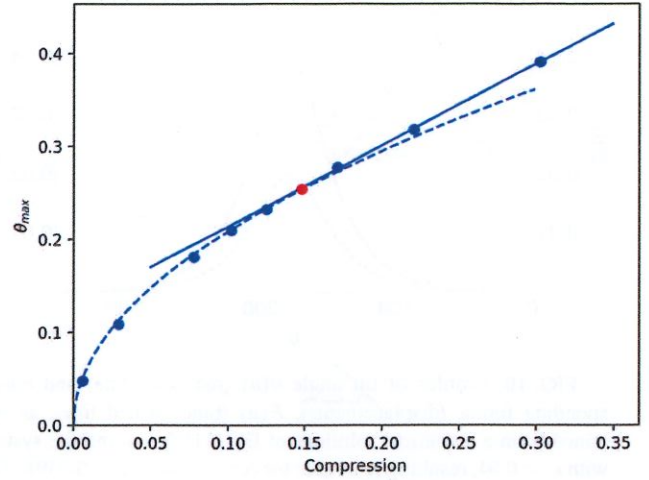


FIG. 14. Variation of θ_{\max} as a function of compression Δ for $N = 10$ as obtained from numerical solutions of the continuous model, Eq. (11). While for low compression $\theta_{\max} \propto \Delta^{1/2}$ (dashed line), for higher compression the variation is linear (solid line). The point marked in red corresponds to the critical value of compression $\Delta_c = \pi/20 \simeq 0.156$, at $\kappa = 0$ ($G_0 = 1/4$), as computed from the first reduced equation for $\kappa = 0$, Eq. (15) [21].

Its value may be estimated using the first reduced equation for $\kappa = 0$, Eq. (15), as $\Delta_c = \pi/(2N)$ [21].

Figure 14 shows that the two regimes i.e., $\kappa^2 \leq 0$ (or $G_0 \leq 1/4$), are significant for the variation of θ_{\max} (and other quantities) on Δ . Whereas for $\kappa^2 > 0$, where the solution approaches that of an infinite system, a roughly linear dependence is found (see Fig. 11), there is roughly a square-root form for $\kappa^2 < 0$ and this may be shown in the exact asymptote form.

The same distinction was seen in the earlier computation for the discrete chain ([18] and Fig. 9), and could be explained directly, but the continuous model provides a relatively transparent interpretation.

VIII. EXPERIMENTS

In the previous sections we have presented a number of numerical results which invite comparison with experiments. In earlier work our interest lay mainly in the many three-dimensional structures found under higher compression and we used a lathe to create a harmonic confining potential [18,20]. Recently we have demonstrated a much simpler experimental setup that is sufficient for the regime considered in this paper. Hard spheres (e.g., ball bearings) placed in a horizontal cylindrical tube exhibit all of the localization properties described here (see [22] for full details). Provided that the diameter of the tube is much greater than that of the spheres, the system is approximately planar. Gravity gives rise to the quadratic potential included in the model. We have used such a system to provide illustrations of the theoretical results of this paper; one was already shown in Fig. 1 for compression $\Delta = 1.04$.

All of these experiments were carried out using eight steel spheres (ball bearings) with diameter $D = 6.33$ mm,

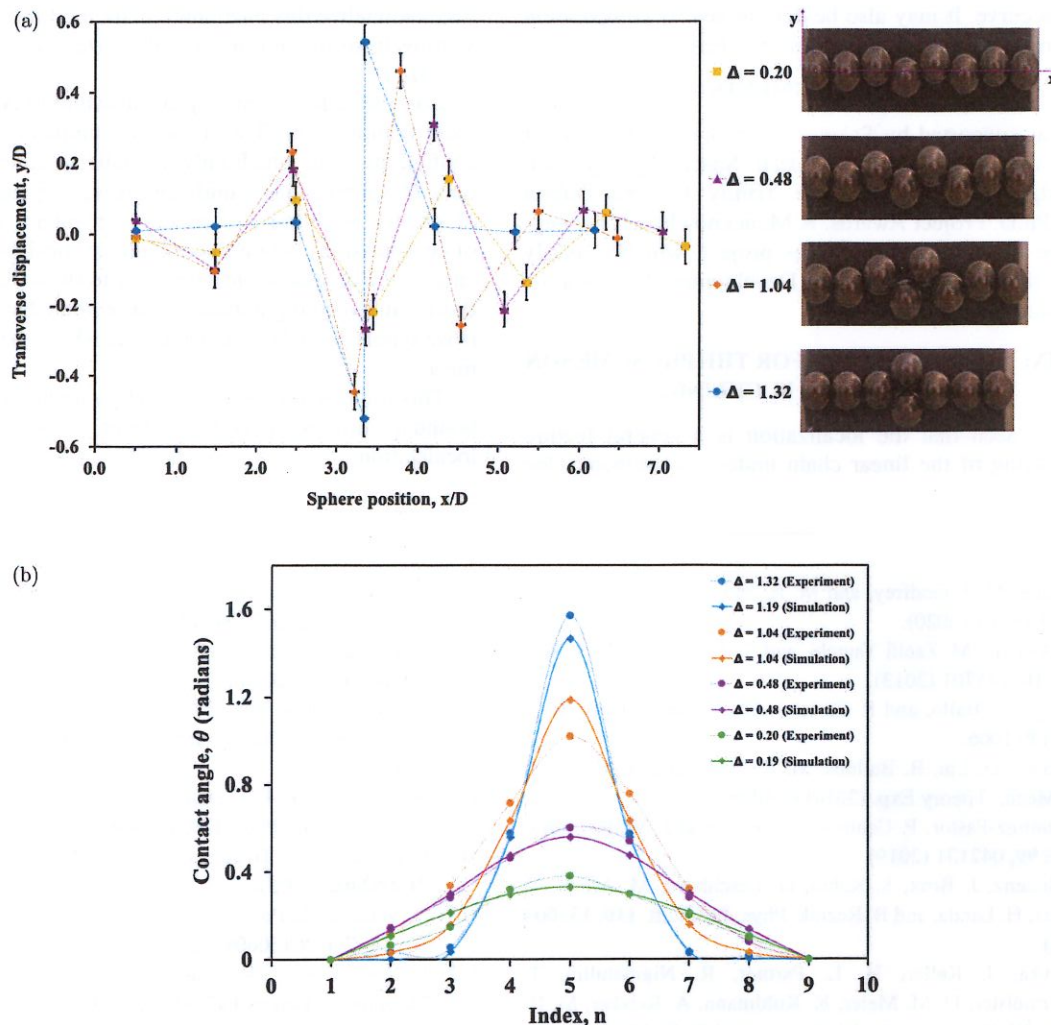


FIG. 15. Experimental data for a chain of $N = 8$ hard spheres for four different values of compression Δ . (a) Transverse displacement profiles. At compression $\Delta = 1.32$ we observe a doublet structure. (b) Profiles of contact angles θ_i for several values of compression. The experimental data are roughly matched by our numerical results.

522 confined in a transparent cylindrical tube with inner diameter
 523 20.05 mm. The tube is closed with stoppers at each end, with
 524 one stopper being movable, so that the tube volume can be
 525 smoothly adjusted in the course of an experimental run. In
 526 order to decrease friction between the spheres we immersed
 527 them in vegetable oil. A small hole in the upper half of the tube
 528 allows for the escape of air, as the stopper is pushed inwards.
 529 A spirit level was used to facilitate horizontal alignment of the
 530 tube. Compression Δ is given by $\Delta = N - L/D$, where L is
 531 the chain length; all our experiments were for $N = 8$ spheres.

532 Figure 15(a) shows a sequence of photographs of a chain of
 533 eight spheres for increasing values of compression. Buckling
 534 is seen to occur around the center of the chain (symmetric
 535 peak); see structure S in our simulations shown in Fig. 7.

536 From image analysis (using IMAGEJ [23]) we are able to
 537 measure positions and hence angles of the structure. The angle
 538 profiles θ_n , shown in Fig. 15(b), are found to be in good
 539 agreement with simulations, of the kind described in Secs. III
 540 and IV. The increase of the maximum tilt angle as a function
 541 of compression, and the corresponding decrease of the width

of the angle profile, feature also in our discrete simulations
 [see Fig. 9(a)].

IX. CONCLUSION

542 We have completed an analysis and interpretation of some
 543 of the key properties of the linear chain of hard spheres under
 544 confinement and compression. Understanding of the system
 545 is fairly complete and it can be said to stand as a prototype
 546 for various physical systems of interest. We have deferred to
 547 a later publication the mathematical developments, involving
 548 Jacobi functions, that are mentioned in Sec. VII.

549 At the same time, it is itself amenable to experiment,
 550 of which we have shown a simple example. One further
 551 experiment we intend to conduct is the investigation of the
 552 Peierls-Nabarro potential. This is the apparent potential, given
 553 as a function of position, experienced by the localized peak of
 554 buckling when it is moved by an added force. It is a contin-
 555 uous potential, including the values for energy for stable and
 556 unstable solutions [e.g., Fig. 4(c)] as minima and maxima of a
 557
 558
 559

need project number
 RETURN 4000129502/20/NL/PS/pt
 MAP Project: (CORA) for MAP Programme
 SciSpace

560 continuous curve. It may also be determined by computation
 561 in an extension of the methods presented here.

562 **ACKNOWLEDGMENTS**

563 S.H. was supported by Science Foundation Ireland Grant
 564 No. 13/IA/1926 and the European Space Agency. A.I.
 565 acknowledges funding from the Trinity College Dublin
 566 Provost's Ph.D. Project Awards. A.M. acknowledges the sup-
 567 port of the Supercomputing Wales project, which is partly
 568 funded by the European Regional Development Fund via the
 569 Welsh Government.

FQ

570 **APPENDIX: WHAT ACCOUNTS FOR THE PHENOMENON**
 571 **LOCALIZATION OF BUCKLING?**

572 We have seen that the localization is a general feature
 573 of the buckling of the linear chain under confinement. One

574 may rationalize this phenomenon by the following argument,
 575 starting from the uniform (nonlocalized) zigzag structure of
 576 Sec. II.

577 Consider a long finite zigzag structure of N spheres under
 578 fixed compression. This is to be compared with a second
 579 configuration, in which only a smaller section, consisting of
 580 only M spheres, has a uniform zigzag structure (necessarily
 581 of greater amplitude, in order to maintain the same value
 582 of compression), while the remainder consists of the straight
 583 chain (zero displacement). It is easy to show that the energy of
 584 this localized configuration is smaller than that of the original,
 585 if we ignore boundary contributions where the two structures
 586 meet.

587 This implies a reduction of energy upon reducing M , until
 588 boundary effects intervene to limit it, in a crude form of
 589 localization.

6

[1] Y. Zhang, M. J. Godfrey, and M. A. Moore, arXiv: Soft Condensed Matter (2020).

[2] S. S. Ashwin, M. Zaeifi Yamchi, and R. K. Bowles, *Phys. Rev. Lett.* **110**, 145701 (2013).

[3] S. Varga, G. Balló, and P. Gurin, *J. Stat. Mech.: Theory Exp.* (2011) P11006.

[4] C. Moore, D. Liu, B. Ballnus, M. Karbach, and G. Müller, *J. Stat. Mech.: Theory Exp.* (2014) P04008.

7

[5] A. Ramirez-Pastor, P. Centres, E. Vogel, and J. Valdés, *Phys. Rev. E* **99**, 042131 (2019).

[6] M. Mielenz, J. Brox, S. Kahra, G. Leschhorn, M. Albert, T. Schaez, H. Landa, and B. Reznik, *Phys. Rev. Lett.* **110**, 133004 (2013).

[7] K. Pyka, J. Keller, H. L. Partner, R. Nigmatullin, T. Burgermeister, D. M. Meier, K. Kuhlmann, A. Retzker, M. B. Plenio, W. H. Zurek, A. del Campo, and T. E. Mehlstäubler, *Nat. Commun.* **4**, 1 (2013).

Q

[8] R. C. Thompson, *Contemp. Phys.* **56**, 63 (2015).

[9] H. L. Partner, R. Nigmatullin, T. Burgermeister, J. Keller, K. Pyka, M. B. Plenio, A. Retzker, W. H. Zurek, A. del Campo, and T. E. Mehlstäubler, *Physica B: Condensed Matter* **460**, 114 (2015).

[10] R. Nigmatullin, A. del Campo, G. De Chiara, G. Morigi, M. B. Plenio, and A. Retzker, *Phys. Rev. B* **93**, 014106 (2016).

[11] L. Yan, W. Wan, L. Chen, F. Zhou, S. Gong, X. Tong, and M. Feng, *Sci. Rep.* **6**, 21547 (2016).

[12] H. Landa, B. Reznik, J. Brox, M. Mielenz, and T. Schätz, *New J. Phys.* **15**, 093003 (2013).

[13] A. Melzer, *Phys. Rev. E* **73**, 056404 (2006).

[14] T. Beatus, T. Tlustý, and R. Bar-Ziv, *Nat. Phys.* **2**, 743 (2006).

[15] A. V. Straube, R. P. A. Dullens, L. Schimansky-Geier, and A. A. Louis, *J. Chem. Phys.* **139**, 134908 (2013).

[16] L. E. Helseth, T. H. Johansen, and T. M. Fischer, *Phys. Rev. E* **71**, 062402 (2005).

[17] D. Vella, E. du Pontavice, C. L. Hall, and A. Goriely, *Proc. R. Soc. A* **470**, 20130609 (2014).

[18] J. Winkelmann, A. Mughal, D. Weaire, and S. Hutzler, *Europhysics Letters* **127**, 44002 (2019).

[19] J. Winkelmann, A. Mughal, D. B. Williams, D. Weaire, and S. Hutzler, *Phys. Rev. E* **99**, 020602(R) (2019).

[20] T. Lee, K. Gizynski, and B. A. Grzybowski, *Adv. Mater.* **29**, 1704274 (2017).

[21] D. Weaire, A. Mughal, and S. Hutzler, (unpublished).

8

[22] D. Weaire, A. Irannezhad, A. Mughal, and S. Hutzler, *Am. J. Phys.* **88**, 347 (2020).

[23] M. D. Abràmoff, P. J. Magalhães, and S. J. Ram, *Biophotonics International* **11**, 36 (2004).

Q